14th International Symposium on Turbulence and Shear Flow Phenomena (TSFP14)
Heidelberg, Germany, July 28–31, 2026

# EXPERIMENTAL INVESTIGATION OF BUBBLE-INDUCED TURBULENCE MODULATION VIA PLANAR PARTICLE TRACKING

**Augusto H. P. Zanca**
Graduate School of Engineering Science
The Univeristy of Osaka
1-3 Machikaneyama, Toyonaka
Osaka, 560-8531, Japan
a_zanca@fm.me.es.osaka-u.ac.jp

**Yutaro Motoori**
Graduate School of Engineering Science
The Univeristy of Osaka
1-3 Machikaneyama, Toyonaka
Osaka, 560-8531, Japan
y.motoori.es@osaka-u.ac.jp

**Susumu Goto**
Graduate School of Engineering Science
The Univeristy of Osaka
1-3 Machikaneyama, Toyonaka, Osaka, 560-8531, Japan
s.goto.es@osaka-u.ac.jp

## ABSTRACT
An experimental investigation of turbulence modulation in liquid phase by air bubbles is conducted through the development of a unique planar particle tracking algorithm. The developed methodology combines previously established techniques such as particle image reconstruction with novel concepts in order to attain a robust and fast tracking algorithm suitable to a diverse range of experimental scenarios. This allows us to conduct planar measurements in bubbly flows without the need for complex multiple camera setups, helping us to gain new insights into these types of phenomena in challenging flow scenarios. In an experimental setting of Taylor–Green-like forced turbulence, we can verify the robustness of the developed algorithm for a variety of scenarios with and without the use of shadow imaging. We demonstrate how the use of particle shadow velocimetry also enables us to detect bubble edges and therefore conduct conditional statistics such as the velocity structure functions in the proximity and away from the bubbles. Moreover, we show that even in more constrained cases where the use of shadow imaging is not possible, a conservative algorithm can also be designed to exclude regions occupied by bubbles and account for their presence in the interpolation of the Lagrangian tracks into a fixed grid. This enables us to obtain the velocity spectra, showing how energy in introduced in different scales in bubbly flows.

## BACKGROUND
In recent years, the study of turbulent flows containing suspensions of bubbles and light particles has gained traction due to the wide applicability of these phenomena in industrial settings. With bubbles, the deformability and high density ratio of the suspended phase leads to complex mutual interactions with the turbulent fields, many details of which are not yet completely understood. Over the years, many studies have focused on the problem of bubble-induced turbulence, leading to important findings such as the well-acknowledged $k^{-3}$ scaling law (Lance & Bataille, 1991), and the creation numerical models of these phenomena (Riboux *et al.*, 2013).

Many real-world cases however involve the introduction of bubbles into already turbulent flow. Previous experimental studies in the field have employed methods such as phase-sensitive hot-wire anemometry (Alméras *et al.*, 2017) and particle tracking with fluorescent tracers or shadow-imaging with multiple cameras (Xu *et al.*, 2025) to study bubbly flow in approximately isotropic turbulence. While instrumental to the field, the range of parameters in these studies has been limited. With this in mind, the present study focuses a unique Taylor-Green-like forced flow and the development of a novel approach to particle tracking focusing on robustness, and dispensing the use of fluorescent tracers or shadow imaging of the bubbles. The method is also suited to the challenging experimental conditions which involve high turbulent intensity and tracer density limitations.

## EXPERIMENTAL DEVICE
In the present study, we conduct an experimental analysis of the turbulence modulation when bubbles are introduced in a Taylor–Green-like forced flow. The experimental device consists of a water tank with four submerged rotating elements, which are arranged in pairs that rotate in opposite directions, as shown in figure 1(a). The rotating elements can be exchanged from cylinders to flat plates with similar chord, which changes the way in which the force drives the flow and also the maximum turbulent intensity. To conduct particle tracking velocimetry, Nylon tracer particles with a diameter of $50\,\mu$m are introduced in the water, and a high-speed camera is pointed at the region between the blades. The particles can be illuminated either via a laser sheet positioned in orthogonally to the viewing axis, or through an LED strobe panel which is positioned in the opposite side of the tank in order to conduct shadow imaging of the particles, such as shown in figure 1(b). The viewing direction is selected to analyze the cross-section of the secondary vortices generated in the mean stretching direction of the main vortices. Air bubbles can be injected into the tank through a configurable injector which is placed at the bottom of tank and connected to an air compressor equipped

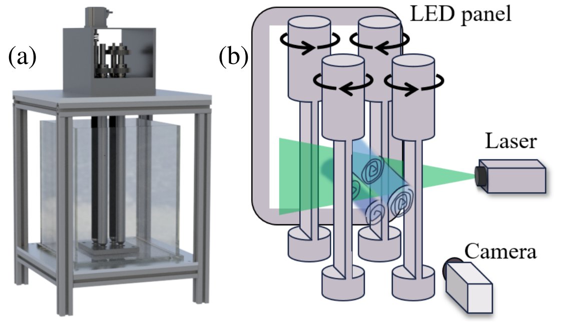


Figure 1. Schematic of experimental apparatus (a) and detail of relative orientation of camera, laser, LED light and rotation speed of the four elements (b).

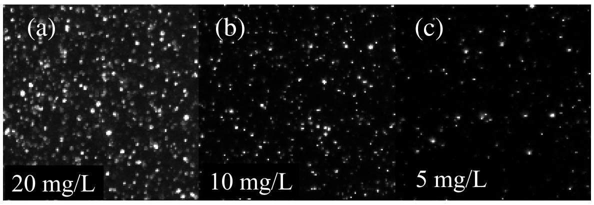


Figure 2. Effect of reduction of image contrast with increasing tracer concentration for (a) 20, (b) 10 and (c) 5 mg/L. Although the tracer used in this image is $10\,\mu$m glass spheres, the effect is the same for the Nylon powder used in the experiment.

with a pressure regulator and a flow-rate meter. It is worth mentioning that for all analyses in this paper, the $x$ and $y$ directions are parallel to the horizontal and vertical, respectively.

One of the challenges with the current experimental device in contrast to jet-driven turbulence or channel-flow setups is the restricted access to the measurement region. Aside from the direct optical obstruction introduced by the blades themselves, the distance from the tank walls to the measurement position (which is used to minimize wall effects in the turbulence generation) imposes an upper limit on the concentration of tracers which can be used before contrast starts to be significantly affected due to light scattering, as shown in figure 2. In practice, average particle separation is comparable to the scale of the smallest eddies for turbulent intensities of the order of $Re_\tau \approx 150$. As a result, PIV based techniques are not adequate for the smallest measurements, and we therefore focus on the use of Particle Tracking Velocimetry (PTV) for our measurements. Another advantage of PTV is the ability to conduct measurements close to interfaces such as bubble edges, one of the main targets of the current study.

## NEW APPROACH TO 2D-PTV

When we consider the problem of particle tracking for bubbly flows, without relying on fluorescent tracers and with a single camera, the use of traditional tracking methods is challenged due to the high number of false detections caused by direct and indirect reflections of the laser light onto bubbles. Additionally, conducting measurements at the stagnation point (characteristic of the current experimental device) and tracer density limitations caused by light scattering meant that a new approach for planar measurements focused on robustness had to be developed. This new approach combines previously established techniques with novel ideas.

### Particle Detection

Detection and discrimination of particles is done through a variation of the Shake-the-Box algorithm (Jahn *et al.*, 2021), which is centered on the iterative reconstruction and optimization of particle images for tracking across multiple-camera systems. The central idea behind Iterative Particle Reconstruction (IPR) methods, stands on the representation of individual particle images through an Optical Transfer Function, traditionally represented as a 2D Gaussian, such as:

$$\mathrm{otf}(u,v) = I e^{-0.5\left(u^2 a + 2buv + cv^2\right)}, \tag{1}$$

where $I$ is the particle image intensity and $a$, $b$ and $c$ the shape parameters, while $u$ and $v$ represent pixel coordinates on the image. The shape parameters can be calibrated for a given experiment, and if the position and intensity of all particles are known, artificial particle images can be rendered into a *reconstructed* (rep) image. A residual, or cost function can be defined as the norm of the difference between this reproduction and original camera image (img):

$$\mathrm{cost} = \sum_{uv} \left|\mathrm{img}_{uv} - \mathrm{rep}_{uv}\right|^2, \tag{2}$$

which is a measure of the quality of the reproduced image against the original. The method consists in an iterative process to detect particles in the original image and optimize their position and intensity by reducing the cost function. Through this process, particle positions are then accurately determined, and since the method works on predefined particle image shapes, overlapping images can also be reliably detected.

Although this method was originally developed for volumetric particle tracking, we show in this study that it can be a very powerful tool in planar tracking scenarios, especially when other objects (such as bubbles) are present in the images. The residual image without particle images, which is a byproduct of the procedure also becomes a key step in the robust detection of bubbles under challenging lighting conditions, such as described in the following section.

For the particle reconstruction to work correctly in these conditions however, some modifications are necessary. In the algorithm proposed by Jahn *et al.* (2021), initial peak detection is conducted via a simple threshold binarization procedure, which works because of the iterative nature of the algorithm (overlapping particles are gradually detected with the removal of detected particle images between successive iterations). The issue is that this leads to false detections when bright, non-particle objects are also present in the images, such as light reflections on bubbles surfaces. While a well-tuned verification step which relies on local image contrast check with successive increase in sensitivity can deal with this issue, the process usually requires many iterations and the resulting algorithm tends to be sensitive to the imaging conditions such as light intensity and tracer concentration.

To solve this, the first change that we propose is to use a correlation-based peak detection scheme in order to find the initial position of particles before the optimization stage. This scheme, which is based on the study of Takehara and Etoh (1999), relies on the calculation of the correlation between a template mask (usually a Gaussian distribution) and the input image. Afterward, a threshold of the correlation value is then used to select the peaks. The advantage of this method is that since it is based on the shape of the particle images and not their peak intensity, it is able to detect tracers

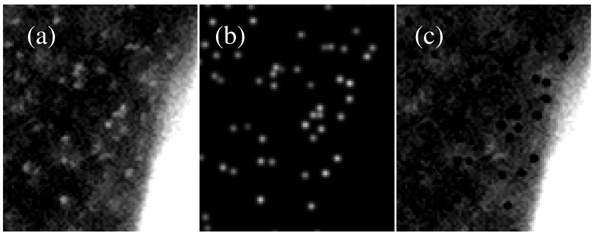


Figure 3. Results of the improved IPR algorithm after three iterations. Zoomed-in original image (a), reproduced image (b) and residual image (c). Bright object in the lower-left corner is a bubble interface.

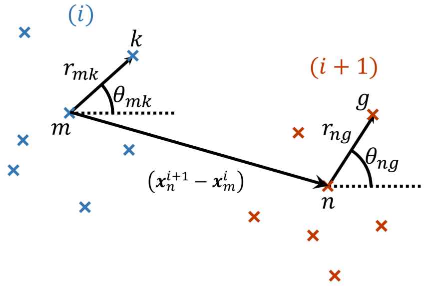


Figure 4. Schematic of particle and neighbor arrangement for the PCSS tracking algorithm.

which are next to or attached to bubble edges. In order to avoid false detections caused by small fluctuations in background intensity, a minimum threshold for peak particle intensity (usually 10 units above background intensity) is selected. Since detections rely only on particle image shapes, this algorithm also requires a smaller number of outer iterations when compared to the original IPR. Usually only 3 iterations (against 20 of the original algorithm) are enough to detect most particles. Results for the detection next to a bubble interface are shown in figure 3 as an example.

One of the traditional disadvantages of this method when compared to the iterative thresholding of the study of Jahn *et al.*, (2021), is that it is sometimes not able to detect particles with similar intensities which are positioned in proximity, such that their images overlap and the combined image is no longer detected by the correlation mask. To remedy this, we increase the mask size for the second iteration, aiming to detect larger blobs of size up to approximately 2 individual particles. This includes most combinations of particles which have not been initially detected, and then the third and final iteration which is conducted again with the smaller mask size captures the images which had been obfuscated in the larger blobs after one of the images has been subtracted. Again, this effect is shown in figure 3, where we can see that the algorithm correctly captures overlapping particles even in challenging noisy conditions.

In the original algorithm, the pixel intensities are interpolated as 2D B-splines, which are then used for the optimization of detected peak positions via a Levenberg-Marquardt algorithm in order to obtain sub-pixel precision and estimate image shapes. Since the optimization is computed for each particle successively, this process can become computationally expensive, in the case of high-resolution images with thousands of particles. To improve this, we eliminate the spline interpolation, and rely on the fitting of a 2D Gaussian curve to the $3\times3$ pixel grid centered on the initial detection, which also results in sub-pixel accuracy to the detections. The implementation of this simpler procedure is possible because the use of the correlation-based peak detection already results in an initial position which is within one pixel or less of the image centroid in most cases. Moreover, since the process is vectorizable, all peak positions can be refined simultaneously.

After initial detection of particle positions, the refinement of position and intensity of the particles is then conducted in the same manner as the base algorithm, with 20 inner optimization iterations for each of the 3 outer iterations. However, contrary to reference study, optimization of the particle intensity and position are conducted is separate blocks across the 20 inner iterations used in the optimization process. In these, the first 5 iterations are used for the intensity alone, and the rest of them for the position optimization, in which the analytical computation of the gradient of the cost function is leveraged. In our experience, this change makes the optimization process more robust against the presence of background light, which can sometimes lead to divergence in the optimization of dimmer particles.

During the inner optimization steps, criteria for minimum intensity and minimum separation are used to filter out possible false detections. As an additional improvement to this filtering stage, we also introduce a mask image which keeps track of which pixels have been filtered out due to intensity or proximity criteria. This mask is then used in the peak detection stage of subsequent outer iterations in order to make the process more efficient by ignoring possible detections in regions which are known to have been excluded due to any of the filtering criteria.

## Particle Tracking

Particle tracking across frames is then done via a variation of the Polar Coordinate-System Similarity (PCSS) method (Shindler *et al.*, 2010). As briefly shown in the schematic of figure 4, for a given particle $m$ in frame $i$, the method attempts to find the particle $n$ in frame $i+1$ which corresponds to the same particle, in order to find a track. We define a polar coordinate-system around the initial particle and calculate the azimuth and distance to all neighbors $k$. In the latter frame, we do the same for all neighbors $g$ of particle $n$. A similarity index between particles $m$ and $n$ is then computed according to (3), where $h$ is a step function equal to 1 when both arguments are positive and equal to 0 otherwise, and $\varepsilon_r$, $\varepsilon_\theta$ are radial and angular tolerances respectively.

$$S_{mn} = \sum_{k=1}^{K}\sum_{g=1}^{G} H\left(\varepsilon_r r^i_{mk} - \left|r^i_{mk} - r^{i+1}_{ng}\right|, \varepsilon_\theta - \left|\theta^i_{mk} - \theta^{i+1}_{ng}\right|\right) \quad (3)$$

Since a minimum of two frames is necessary, this algorithm is well-suited for short particle tracks. In practice, we introduce improvements such as prediction of particle paths to limit search regions, as well as possibility to search for a suitable particle two frames ahead of the first in case a suitable candidate is not found. These characteristics make this framework useful for the current experimental conditions, where the presence of bubbles can lead to flickering particle images. In contrast with the original algorithm however, we eliminate the introduction of "ghost" particles at interpolated positions when a frame is skipped. Instead, particle tracks are allowed to have non-uniform frame spaces, and the stencils of finite difference used in path prediction and velocity calculations are adapted to account for any missing frames while maintaining second-order accuracy.

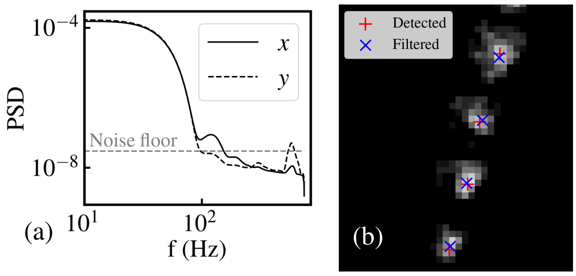


Figure 5. (a) Power Spectrum of tracked particle positions, showing the noise floor. (b) Section of detected trajectory and respective particle images showing initially detected and filtered positions.

The main improvement introduced in the current study for this method is the sequence of computation. In the original method, particles are operated sequentially, where at first the similarity index of all candidates in the search region is compared and then the candidate with the highest similarity is selected. For subsequent particles, conflicts with already selected candidates can occur, meaning that a recursive logic has to be implemented to correctly judge which candidate can be assigned to each particle. To improve this, we compute the similarity indexes of all candidates of all particles first, assigned each particle to their respective best candidate, and deal with conflicts afterward. In this configuration, the computation of the similarity indexes can be vectorized and parallelized, which greatly improves the performance of the algorithm. We also maintain the fallback for the search two frames ahead, and introduce a new one where the predicted position information is ignored in the case of short trajectories, since the likelihood of an erroneous prediction is higher for trajectories which are short (three frames for example).

After tracks have been identified, the noise in the determination of particle positions can be filtered out via the use of a Wiener filter (Wiener, 1949). For the calculation of the filter, the average PSD of the tracer positions is used. The noise spectrum is then approximated as a constant spectrum with power equal to the noise floor at the lowest frequency for which the noise starts to dominate, such as shown in figure 5(a). An example of a few segments of a particle track before and after filtering is presented in figure 5(b). This figure also shows the superimposed particle image throughout the frames of the trajectory, in order to demonstrate that this noise comes not from the determination of the particle image centroid (a procedure which is carried out accurately though the IPR algorithm), but that the noise is contained in the movement of the particle image itself. The authors hypothesize that this is caused by irregularities in particle shape or the interference of other nearby particles which might alter the light scattering of the target particle. The velocity calculations benefit from the elimination of this noise in the position data since it tends to be greatly amplified in the calculation of the derivatives.

In order to obtain fixed-point statistics such as the powerspectrum, results can be transferred to a uniform grid via adaptive Gaussian interpolation. However, since interpolation can lead to smoothing of the results and inability to accurately capture features close to interfaces, it is desirable to conduct analyses with the Lagrangian data whenever possible. To obtain spatial derivatives at a given particle for example, we employ the method described in the study of Qi *et al.* (2025), which consists in the least-squares fitting of a polynomial approximation of the flow field considering a given number of neighbors around each particle. This method is able to deal with the presence of interfaces or non-uniform particle spacings, and also can be tuned for the desired order of accuracy. In order to calculate two-point statistics such as the velocity structure functions and autocorrelation functions, we employ the use of an original directional binning method, where for each tracked particle, we search for possible computation pairs in a narrow corridor which is divided into bins, such as shown in figure 6 for the $x$ direction statistics. By refining the bin size and corridor width, we can obtain more precise results than what would be possible through the interpolation into a fixed grid.

Although bubble edges can be identified somewhat reliably for shadow imaging through a variety of methods which are out of the scope of this paper, the situation becomes more challenging when only the laser illumination is used, where in many cases edges become smoothed or even invisible. To deal with this in a robust manner, an original framework, which is shown in figure 7, has been developed based on simple image processing techniques. After detected particle images are subtracted from the input [figure 7(a)], the process begins with the creation of a bubble mask image by thresholding of image gradients, in order to provide a rough estimate of bubble positions [figure 7(b)]. This is then combined with a Delaunay triangulation based on detected particle positions [figure 7(c)], in which triangles which intersect with the previously calculated mask are considered to be invalid regions and excluded from the interpolation [figure 7(d)]. Although somewhat conservative, this approach results in a robust scheme for the elimination of bubbles and other artifacts considering the single camera and laser setup of the current experiment.

## RESULTS

As examples to evaluate the performance of the developed methods against bubbly flows, we present two distinct experiments. In the first experiment, the shadow imaging technique is used to capture both particle positions and bubble edges simultaneously without the need for the laser sheet. This technique, which is also known as particle shadow velocimetry (Ma *et al.*, 2022) relies on the depth of the focal plane of the camera lens in order to image only a thin slab of the experimental volume. This method allows for both the particle images and the bubble edges to be visible, such as shown in figure 8, but requires a clear line of sight from the camera to the opposite side of the tank, where the light panel must be positioned. We conduct our observations in the central stagnation region between the cylinders, where the analyzed statistics are approximately homogeneous across the viewing area.

For this experiment, we consider two cases utilizing the cylindrical blades with a rotation rate of 15 Hz, and differing in that one of the cases has air injection at a rate of 1 L/s from the bottom of the tank while the other is conducted without air injection. Using a simple edge detection based on image gradients, we can identify bubble edges which are in focus and therefore compute the velocity structure function conditionally to better study the turbulence produced in the wake of the bubbles, such as shown in figure 9(a). The longitudinal second-order structure functions are presented in figures 9(b,c). It is worth mentioning that while the VSFs do follow the $r^{2/3}$ trend closely in the inertial range, the trend of $r^2$ is not observed for small separations. We consider that this is an effect of the thickness of the focal plane, which introduces a decorrelatory effect in the velocity of particles which appear to be in the same position from the point of view of the camera.

From the results, we notice that when the conditional

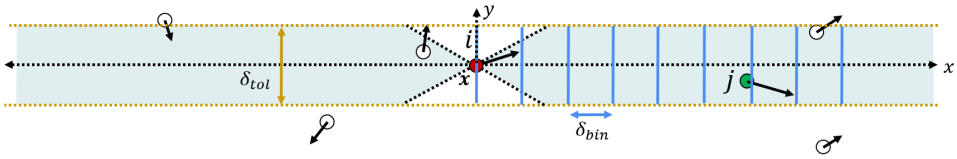


Figure 6. Directional binning schematic for the computation of directional statistics from Lagrangian tracking data.

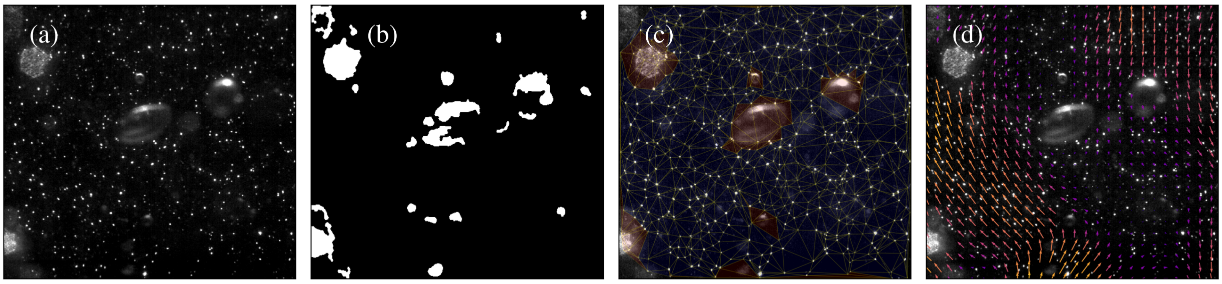


Figure 7. Process of identification of bubbles and artifacts: (a) original image, (b) gradient mask, (c) combination with Delaunay triangulation, (d) and final interpolated field.

Figure 8. Cropped snapshot showing simultaneous imaging of tracer shadows and bubble interfaces.

computation is not considered, the effect of the bubbles is mainly perceived as an increase in turbulent energy throughout the flow, but the scaling of the VSF remains largely unaffected. When we consider the conditional computation however, the modulation becomes more apparent. For the horizontal direction [figure 9(b)], we see that while the single-phase flow follows the expected $r^{2/3}$ scaling for scales comparable to bubble diameter, the curve becomes steeper for the region inside the bubble wake. This observation is consistent with the fact that the energy cascade spectrum becomes steeper inside bubble-induced turbulent wakes, and a similar phenomenon was also observed in the experimental investigation of Ma *et al.* (2025).

Although not included here for brevity, it is a characteristic of the current experimental device that the turbulent intensity on the vertical direction is weaker than in the horizontal. This can be seen in the single-phase curve of figure 9(c), where the VSF has a shallower inclination than the expected inertial scaling. In the bubble wakes however, we can see how the turbulent intensity becomes strong enough for the scaling to be achieved across over a decade of separation distances, for sizes comparable to bubble diameters.

In the second experiment, we consider the more challenging case where the back illumination cannot be used. We analyze three cases in which the flat blades are spun at a rate of 10 Hz, and air is injected with rates of 0 L/s (single-phase), 1 L/s, and 5 L/s. Contrary to the previous case, we conduct the analysis in this experiment through the conservative masking strategy described earlier and shown in figure 7, combined with the interpolation of the results into a fixed grid, from which the power spectra of the flow can be calculated. To account for the presence of bubbles, the PSD is obtained via an estimate of the autocorrelation function, a method which is known to produce reliable results for interrupted measurements (Dorseth *et al.*, 2024). We show the PSD separated by experimental case [figure 10(a)] and velocity component [figure 10(b)].

It is notable from the PSD results that the difference between the components at the lower frequencies is intensified as the air injection is increased, with the $y$ component seeing slight attenuation of energy in this region. At the medium and higher frequencies, both components show a similar increase in energy. This indicates that the slight attenuation in the lower frequencies is balanced by the increase in energy across the remaining parts of the spectrum, resulting in the overall increase in turbulent energy.

## CONCLUSIONS

The present study focuses on the experimental analysis of turbulence modulation by bubbles through the development of a novel planar particle tracking approach. The new algorithm allows us to conduct measurements robustly with varying air fraction rates without the need for multiple cameras or fluorescent tracers. This is achieved through the introduction of novel concepts into previously established techniques in order to gain new insight in these complex phenomena in a way which was not possible until now.

The implementation of a correlation-based peak detection scheme as well as simpler initial optimization steps allows us to detect tracer particles with high confidence even in dense imaging conditions and in the presence of bubbles. During particle tracking, a reformulation of the logic in the polar coordinate-system similarity tracker results in a faster algorithm which accounts for short tracks and flickering particle images. From this, a unique two-point statistics calculation scheme and robust bubble detection strategies allow us to post-process these results even in challenging lighting conditions where the use of shadow imaging is not possible.

To test these new methods, we presented two distinct experimental conditions. With the use of particle shadow velocimetry, we can detect bubble edges which are in focus in

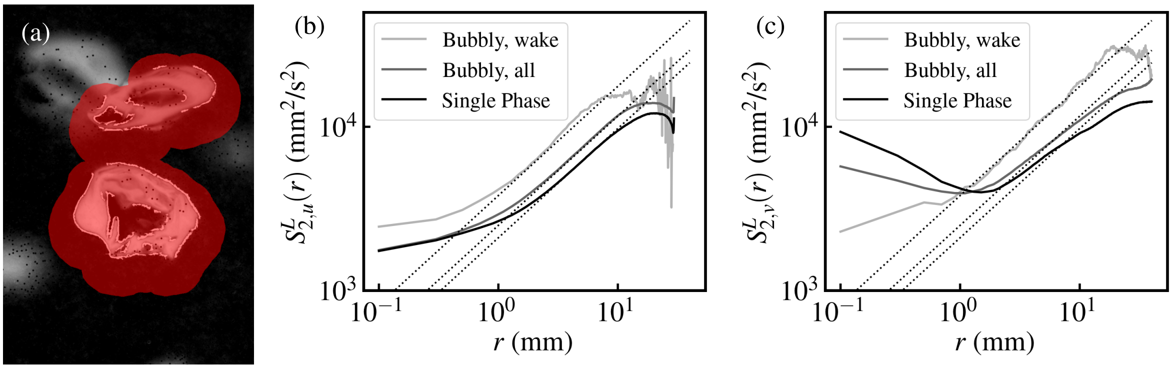


Figure 9. Detected bubble edges in focus superimposed on residual image, with area for conditional calculation in red (a). Longitudinal horizontal (b) and vertical (c) second-order velocity structure function for the cases without and with bubbles, including conditional calculation Dotted line represents $r^{2/3}$ scaling.

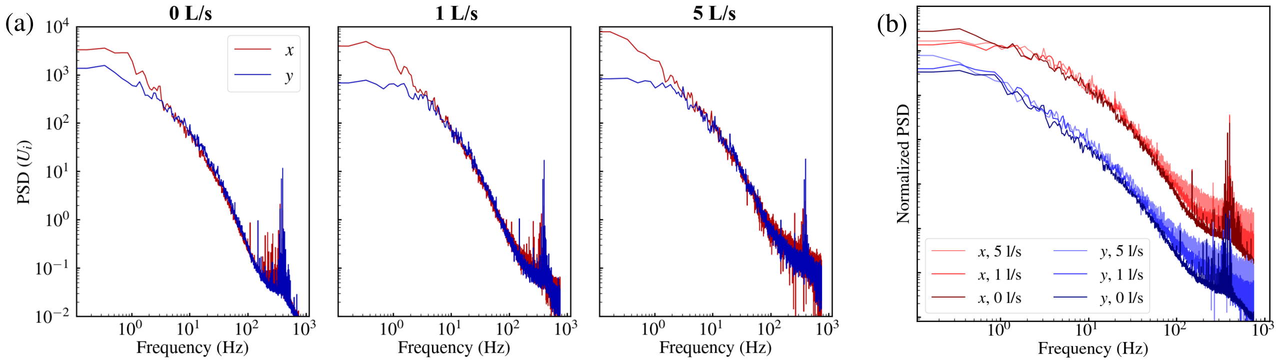


Figure 10. Comparison of Power Spectral Density of velocity measurements separated by: (a) air injection rate and (b) coordinate direction.

order to conditionally compute the longitudinal velocity structure functions. The obtained results indicate how energy is introduced in scales comparable to bubble diameter, modifying the energy cascade. In a second experiment, we show how even in the absence of background illumination, the conservative bubble detection strategy allows us to correctly calculate the energy spectra from the autocorrelation functions. The results indicate that for the current bubble fractions, the effect in the energy cascade is small, and energy is mostly injected or extracted at the low frequencies, with an anisotropic effect across both directions.

Overall, the results indicate that even in challenged and limited experimental conditions, adequate methods have been developed to conduct accurate planar measurements of complex two-phase flow interactions. These methods pave the way to more detailed analyses and a more complete understanding of the modulation of turbulence due to bubbles in the future.

## ACKNOWLEDGEMENTS

This study was partly supported by the JSPS Grant-in-Aid for Scientific Research Grant Numbers 25K01158, 26K17306 and by JSPS Grant-in-Aid for Transformative Research Areas Grant Number JP26H00389.

## REFERENCES

Alméras, E., Mathai, V., Lohse, D. & Sun, C. 2017 Experimental investigation of the turbulence induced by a bubble swarm rising within incident turbulence. *Journal of Fluid Mechanics* **825**, 1091–1112.

Dorseth, M., Perez, J. C., Bourouaine, S., Palacios, J. C. & Raouafi, N. E. 2024 The low-frequency power spectrum of slow solar wind turbulence. *Astronomy & Astrophysics* **689**, A117.

Lance, M. & Bataille, J. 1991 Turbulence in the liquid phase of a uniform bubbly air–water flow. *Journal of Fluid Mechanics* **222**, 95–118.

Ma, T., Hessenkemper, H., Lucas, D. & Bragg, A. D. 2022 An experimental study on the multiscale properties of turbulence in bubble-laden flows. *Journal of Fluid Mechanics* **936**, A42.

Ma, T., Tan, S., Ni, R., Hessenkemper, H. & Bragg, A. D. 2025 Kolmogorov Scaling in Bubble-Induced Turbulence. *Physical Review Letters* **134** (24), 244001.

Qi, Y., Li, Y. & Coletti, F. 2025 Small-scale dynamics and structure of free-surface turbulence. *Journal of Fluid Mechanics* **1007**, A3.

Riboux, G., Legendre, D. & Risso, F. 2013 A model of bubble-induced turbulence based on large-scale wake interactions. *Journal of Fluid Mechanics* **719**, 362–387.

Shindler, L., Moroni, M. & Cenedese, A. 2010 Spatial–temporal improvements of a two-frame particle-tracking algorithm. *Measurement Science and Technology* **21** (11), 115401.

Wiener, N. 1949 *Extrapolation, Interpolation, and Smoothing of Stationary Time Series*, 1st edn. Cambridge, MA: MIT Press.

Xu, X., Tan, S., Qi, Y. & Ni, R. 2025 Experimental investigation of turbulence modulation by deformable bubbles. *Physical Review Fluids* **10** (3), 033605.